Eur. Phys. J. E (2014) **37**: 129
DOI 10.1140/epje/i2014-14129-7

THE EUROPEAN PHYSICAL JOURNAL E

Regular Article

Hierarchical structure in microbial cellulose: What happens during the drying process

Yue Zhao[1,a], Satoshi Koizumi[1,2,b], Daisuke Yamaguchi[1], and Tetsuo Kondo[3]

[1] Quantum Beam Science Center, Japan Atomic Energy Agency (JAEA), Tokai, Ibaraki 319-1195, Japan
[2] Engineering Department, Ibaraki University, Hitachi, Ibaraki 316-8511, Japan
[3] Bio-Architecture Center & Graduate School of Bioresource and Bioenviromental Science, Kyushu University, Fukuoka 812-8581, Japan

Received 8 May 2014 and Received in final form 27 October 2014
Published online: 29 December 2014 –

Abstract. We present a time-resolved investigation of the natural drying process of microbial cellulose (MC) by means of simultaneous small-angle neutron scattering (SANS), intermediate-angle neutron scattering (IANS) and weighing techniques. SANS was used to elucidate the microscopic structure of the MC sample. The coherent scattering length density of the water penetrating amorphous domains varied with time during the drying process to give a tunable scattering contrast to the water-resistant cellulose crystallites, thus the contrast variation was automatically performed by simply drying. IANS and weighing techniques were used to follow the macroscopic structural changes of the sample, *i.e.*, the composition variation and the loss of the water. Thus, both the structure and composition changes during the whole drying process were resolved. In particular, the quantitative crosscheck of composition variation by IANS and weighing provides a full description of the drying process. Our results show that: i) The natural drying process could be divided into three time regions: a 3-dimensional shrinkage in region I, a 1-dimensional shrinkage along the thickness of the sample in region II, and completion in region III; ii) the further crystallization and aggregation of the cellulose fibrils are observed in both the rapid drying and natural drying methods, and the rapid drying even induces obvious structural changes in the length scale of 7–125 nm; iii) the amount of "bound water", which is an extremely thin layer of water surrounding the surfaces of cellulose fibrils, was estimated to be ~ 0.35 wt% by the weighing measurement and was verified by the quantitative analysis of SANS results.

1 Introduction

Microbial cellulose (MC) synthesized by bacteria *Acetobactor Xylinum*[1] is reported to be exceptionally pure containing no additional components of hemicellulose, lignin or other substances [1–3]. It is a supramolecular system, absorbing large amount of water up to $\sim 99\%$ by weight. This high water-holding ability is closely related to its hierarchical structures. In our previous study [4,5], we examined the hierarchical structure in water-swollen MC membrane over a wide range of length scales from 7 nm to 10 μm by using an ultra-small–angle neutron scattering technique.

Our study showed that the scattering intensity of the MC membrane, $I(q)$, and the magnitude of the scattering vector, q, obey the power law behavior, owing to the mass fractal due to the distribution of the center of mass for the cellulose crystallites in the amorphous phase swollen by water. As q increases, the power law exponent, α, takes the values of 2.5, 1, and 2.4, corresponding to a gel network composed of bundles, a bundle composed of cellulose ribbons, and concentration fluctuations in a bundle. From the mass fractal q-behavior and its length scale limits, we obtained the following pieces of evidence: The network contains 75 vol. % of water and 25 vol. % of the bundles; the bundles contain 91 vol. % of water and 9 vol. % of ribbons; and the ribbons contain 95 vol. % of water and 5 vol. % of microbial cellulose fibrils. In this work, we advance this study and aim to investigate the hierarchical structure and structural change in the MC membrane during the drying process.

As we know, MC exhibits many well-known unique physical properties such as high elasticity, high crystallinity in the dried state, and superior mechanical strength [6–8]. Due to these features, MC is used as electronic paper display [9], metal catalysts carrier [10],

[a] e-mail: zhao.yue@jaea.go.jp
[b] e-mail: skoizumi@mx.ibaraki.ac.jp

[1] A typical Hestrin-Schramm culture medium (pH $\sim$ 6.0) was used in this study (%, w/v): glucose, 2.0; peptone, 0.5; yeast extract, 0.5; disodium phosphate, 0.27; citric acid, 0.115; H_2O, 96.615.

acoustic membranes in speakers [11], artificial blood vessels [12,13] and wound dressing [14–20]. Up to now, there have been plenty of reports on the physical and mechanical properties of MC membranes in both wet and dried states [9–22]. Particularly, studies aiming to investigate how the structure of MC membranes changes by drying and whether the change can be properly controlled, have attracted much attention lately because such information is very crucial for the structure, performance and applications of MC membranes [21,22]. Clasen *et al.* [21]. have studied morphologies of the dried MC membranes via different drying methods (slow evaporation or freeze-drying), by using IR-spectroscopy and scanning electron microscopy (SEM) techniques. They pointed out that the porous network structure of MC membranes is destroyed in the slow evaporation process due to the aggregation of cellulose strands, whereas the structure can be maintained in the freeze-drying process. These results were confirmed in a recent report by Zhang *et al.* [22], where they also found that when compared with the hot air drying, freeze-drying shows reduced strength of hydrogen bonds between cellulose macromolecules and the degree of crystallinity of the dried MC membranes, but had little influence on the crystal structures, hence the mechanical properties of MC membranes prepared by freeze-drying are lower. Studies on other sources of cellulose whiskers prepared from wood or cotton showed that though the drying method slightly influences the crystal structure and the crystallinity, it does affect the nanoscale structure considerably [23].

In this work, we investigated *in situ* the drying process of MC membranes. The original wet MC samples were prepared by the standard Hestrin-Schramm (HS) method (see footnote [1]) as will be detailed in the Experimental section, then they were dried in a silica gel desiccator (natural drying) or in a vacuum oven (rapid drying) under controlled conditions. We follow the natural drying process by time-resolved weighing and neutron scattering techniques. The weighing technique is used to measure the remaining weight of the sample during the drying process, reflecting the macroscopic structural changes. Neutron scattering is used to detect the scattering intensity, $I(q)$, as a function of q, which is defined by $q = (4\pi/\lambda)\sin(\theta/2)$, with λ and θ being the wavelength and scattering angle, respectively. In a single scattering measurement, the small-angle neutron scattering (SANS) intensity profile at small q range and the intermediate-angle neutron scattering (IANS) intensity profile at large q range are obtained simultaneously. The SANS profile is q-dependent and used to elucidate the microstructure of MC. Note that the water can penetrate and swell the non-crystalline cellulose regions, therefore the averaged scattering length density of the water penetrating amorphous regions changes when water evaporates during the drying process. Therefore, the scattering contrast between cellulose crystallites and amorphous regions varies upon drying, and offers an automatically simple way of contrast variation to clarify the microstructures. The IANS profile is q-independent and used to describe the incoherent scattering intensity of the sample, which is similar and complementary to the result obtained by the weighing technique and represents the macroscopic structural changes. Since the incoherent scattering intensity is proportional to the number of hydrogen atoms irradiated by neutrons in the scattering volume, it is affected by any changes in the number density of hydrogen atoms in the system, such as the dimensional change of the sample and the evaporation of the protonated water (H_2O) from the sample.

It is worthy to note the unique points of using neutron as a probe in this study as follows: i) the scattering contrast between the cellulose crystallites and the amorphous regions is tunable due to the decrease in water concentration caused by drying. Thus the contrast variation can be easily achieved without any extra procedures. Furthermore, the pathway of the change in the scattering contrast depends on by using either protonated water (H_2O) or deuterated water (D_2O) as the solvent. ii) The cross-check of both IANS and weighing techniques enables us to quantitatively interpret the composition change during the whole drying process.

2 Experimental

2.1 Sample preparation

A MC pellicle (the continuous film formed on the surface of the culture solution) with a thinness of $\sim 10\,\mathrm{mm}$, was cultivated in the HS culture solution with a quiescent condition (see footnote [1]). The detailed cultivation process can be found elsewhere [4,5,24,25]. The MC pellicle contains dry cellulose fibrils of $\sim 1\,\mathrm{wt\%}$ and water of $\sim 99\,\mathrm{wt\%}$, which was estimated by the weight measurements of the same piece of sample in the original wet state and in the completely vacuum-dried state. MC membrane samples used in this study were prepared by cutting the pellicle on the air side of the culture solution into square-shaped slices of $40 \times 30\,\mathrm{mm}^2$. The thickness of the sample, x_0, is $\sim 2.6\,\mathrm{mm}$, which was calculated from the weight, height and width measurements[2]. We studied three pieces of samples in this work, designated as samples 1–3. Sample 1 was used directly in the following experiments without washing, whereas samples 2 and 3 were pretreated by immersing and washing in a large amount of D_2O for a week in order to completely replace free protonate water (H_2O) with D_2O and to remove the organic compounds and salts.

Samples 1 and 2 were dried naturally in a desiccator filled with silica gel at room temperature for 10 hours (natural drying method) as shown in fig. 1, the process

[2] It has been confirmed that a MC gel contains $\sim 99\,\mathrm{wt\%}$ water and $\sim 1\,\mathrm{wt\%}$ dried cellulose fibrils [26,27]. Thus it is reasonable to assume that the density of a swelling MC gel is equal to that of water, *i.e.*, $d_{\mathrm{MC}} \sim 1.0\,\mathrm{g/cm^3}$ for sample 1 and $d_{\mathrm{MC}} \sim 1.1\,\mathrm{g/cm^3}$ for samples 2 and 3, respectively. Since the across area (A) of each specimen is prescribed to be $3 \times 4\,\mathrm{cm}^2$, the original thickness (x_0 in cm) of the sample can be estimated from the original weight of the sample (W_0 in g) as follows: $x_0 = W_0/(d_{\mathrm{MC}}A) = W_0/(12d_{\mathrm{MC}})$. Note that W_0 is 3.1279, 3.4119 and 3.4261 g for samples 1, 2 and 3, respectively. Therefore, x_0 for samples 1, 2 and 3 is $\sim 0.26\,\mathrm{cm}$.

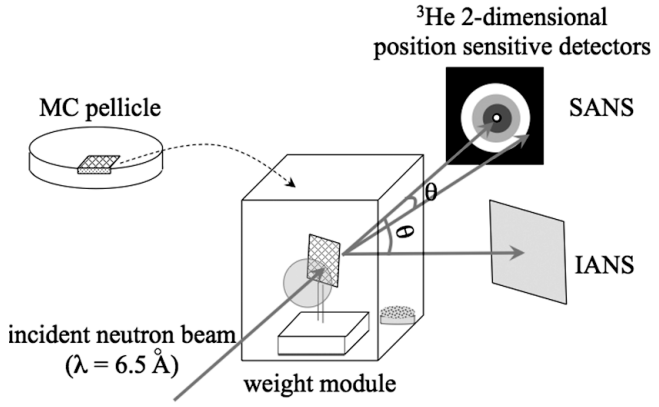

Fig. 1. Schematic illustration of simultaneous time-resolved SANS, IANS and weighing measurements for one MC sample.

of which was investigated by simultaneous time-resolved techniques of weighing and neutron scattering. Sample 3 was dried in the vacuum oven (rapid drying method) at room temperature, and its microstructure before and after drying was investigated by the neutron scattering technique.

2.2 Time-resolved neutron scattering at small angle and intermediate angle

The MC sample was placed on the frame in such a way that the normal vector of the sample was parallel to the incident neutron beam, and on the stage of the weighing balance where time-resolved neutron scattering and weighing measurements can be performed simultaneously (see fig. 1 and the details described below). SANS and IANS measurements were performed on a focusing ultra-small-angle neutron scattering (USANS) instrument, SANS-J-II, at research reactor JRR-3, JAEA, at Tokai, Japan [28]. The incident neutron beam is mono-chromatized by a velocity selector to have average wavelength $\lambda = 6.5\,\text{Å}$ and the wavelength distribution, $\Delta\lambda/\lambda \sim 12\%$. The scattered neutrons were detected with two 2-dimensional ^{3}He position-sensitive detectors: one is for SANS equipped at $\theta = 0°$, covering scattering angles at $0 < \theta < 6.4°$, and the other is for IANS equipped at $\theta = 31°$, covering scattering angles at $23.6° < \theta < 38.4°$.

The 2-dimensional SANS pattern was circularly averaged to obtain the scattering intensity profile, $I(q)$, as a function of q. $I(q)$ was corrected for background scattering, electronic noise of the detector, and for detector sensitivity. After calibration by the secondary standard sample of porous aluminium and the transmission, $I(q)$ was in the absolute unit (cm^{-1}) [28].

In an IANS measurement, the circular-averaged scattering intensity was found to be q-independent, and believed to be the incoherent scattering intensity dominantly. To simplify the discussion, we hereafter used the total counts of neutrons which arrived in the IANS detector per unit time, N, to represent the incoherent scattering intensity, I_{inc}. N is proportional to I_{inc} and describes the number of hydrogen atoms in the scattering volume.

Note that SANS-J-II has both conventional pinhole SANS collimation which covers $0.003 < q < 0.1\,\text{Å}^{-1}$ and focusing USANS collimation which is achieved with MgF_2 lenses and covers $3\times10^{-4} < q < 3\times10^{-3}\,\text{Å}^{-1}$. In order to reach a q-region of $10^{-5}\,\text{Å}^{-1}$ order, double crystal (Bonse-Hart) USANS spectrometer @ PNO in JRR-3 was also utilized in this study [29], where q could be extended to the range of $3\times10^{-5} \sim 3\times10^{-4}\,\text{Å}^{-1}$ by using grooved perfect silicon crystals and thermal neutrons with $\lambda = 2\,\text{Å}$. The combination of SANS-J-II and PNO offers us a chance to observe the entire hierarchical structures of an MC sample.

2.3 Time-resolved weighing measurement

In order to follow the weight loss during the drying process, a weight module (Mettler Toledo, WXSS205DU) was placed on the neutron beam line, so that the neutron scattering and weighing measurements could be performed simultaneously. Figure 1 schematically shows the experimental setup schematically, where both the MC sample and the weight module were sealed in the desiccator, where windows for the neutron beam to pass through were made of thin aluminium sheets to minimize the noise level in the scattering measurements.

A residual weight fraction, $W(t)$, is defined by $W(t) = m_t/m_0$, where m_t and m_0 represent the weight of the sample at time t and 0, respectively. Using $W_{\text{s}}(0) = 0.99$ and $W_{\text{c}}(0) = 0.01$ as the weight fractions of the solvents and dry cellulose fibrils at $t = 0$, $W(t)$ is related to the residual weight fraction of the solvents, $W_{\text{s}}(t)$, and the volume fraction of the solvents, $\phi_{\text{s}}(t)$, at a given t, as follows:

$$W(t) = W_{\text{s}}(t) + W_{\text{c}}(0) = \phi_{\text{s}}(t)d_{\text{s}} + 0.01, \qquad (1)$$

where d_{s} is the mass density of the solvents. Since water is the dominant component in the culture solution, it is reasonable to assume that $d_{\text{s}} = 1.0\,\text{g/cm}^3$ for sample 1 (in H_2O) and $d_{\text{s}} = 1.1\,\text{g/cm}^3$ for sample 2 (in D_2O), thus $\phi_{\text{s}}(t)$ is deduced from eq. (1) as below:

$$\phi_{\text{s}}(t) = W(t) - 0.01 \qquad (2)$$

for sample 1, and

$$\phi_{\text{s}}(t) = [W(t) - 0.01]/1.1 \qquad (3)$$

for sample 2. $\phi_{\text{s}}(t)$ obtained here in eqs. (2) or (3) is a key parameter in calculating the scattering length density of the amorphous regions (ρ_{amo}) to be described in the next sect. 2.4, and to measure the change of N upon drying to be discussed in sect. 3.4.

2.4 Scattering law and contrast variation due to the water evaporation

SANS measurements performed at $0.003 < q < 0.1\,\text{Å}^{-1}$, correspond to a length scale ($= 2\pi/q$) of $7 \sim 200\,\text{nm}$, and

relate to microstructures of MC: the concentration fluctuations of cellulose crystallites in a bundle [4,30]. Let us consider $S(q)$ and $F(q)$ as the structure factor and the form factor of cellulose crystallites. Then $I(q)$ is given by [31,32]

$$I(q) = \Delta\rho^2 \phi_{\rm cc}[1-\phi_{\rm cc}]S(q)F(q), \tag{4}$$

where $\Delta\rho$ is the scattering contrast, which is the difference between the scattering length density (SLD) of the cellulose crystallites ($\rho_{\rm cc}$) and that of the amorphous regions ($\rho_{\rm amo}$) given by

$$\Delta\rho^2 = (\rho_{\rm cc} - \rho_{\rm amo})^2, \tag{5}$$

$\phi_{\rm cc}$ is the volume fraction of cellulose crystallites. During the drying process, both $\Delta\rho^2$ and $\phi_{\rm cc}$ are functions of time. Since amorphous regions include non-crystalline cellulose fibrils and solvents, $\rho_{\rm amo}$ is an averaged SLD of these components, and given by

$$\rho_{\rm amo} = \frac{\phi_{\rm s}\rho_{\rm s} + \phi_{\rm NC}\rho_{\rm NC}}{1-\phi_{\rm cc}}, \tag{6}$$

Here ρ_x and ϕ_x denote the SLD and volume fraction of x [x = NC (non-crystalline cellulose), s (solvent)] at a given time, respectively. $\phi_{\rm NC}\rho_{\rm NC}$ is negligibly small because $\phi_{\rm NC}$ is very small. For a MC sample before drying, $W_{\rm c}(0) = 0.01$. If the crystallinity of MC is assumed to be ~ 0.6 [26], the volume fraction of cellulose crystallites at $t = 0$, $\phi_{\rm cc}(0)$, is estimated to be $\phi_{\rm cc}(0) = W_{\rm c}(0)\times 0.6/d_{\rm c} = 0.0038$, where $d_{\rm c}$ ($\sim 1.58\,{\rm g/cm^3}$) is the mass density of the dried cellulose [27]. Thus $\phi_{\rm cc}$ can be calculated in terms of W as a function of time by

$$\phi_{\rm cc}(t) = W_{\rm c}(0) \times 0.6/(W d_{\rm c}) = \phi_{\rm cc}(0)/W = 0.0038/W. \tag{7}$$

The SLD (ρ) of a molecule of i atoms may be readily calculated from the simple expression below

$$\rho = \sum_i b_i \frac{{\rm d}N_{\rm A}}{M_w}, \tag{8}$$

where b_i is the scattering length of the i-th atom, d is the mass density of the scattering body, M_w is the molecular weight, and $N_{\rm A}$ is the Avogadoro constant [31,32]. We consider water as the only solvent swelling samples 1 and 2, thus the $\rho_{\rm s}(\times 10^{10}\,{\rm cm^{-2}})$ values for H_2O in sample 1 and D_2O in sample 2 are calculated to be -0.56 and 6.34, respectively. Putting these values and eqs. (2), (3), (6) and (7) into eq. (5), we have $\Delta\rho^2$ as follows:

$$\Delta\rho^2 = \left[\rho_{\rm cc} + \frac{0.56w(w-0.01)}{(w-0.0038)}\right]^2 \tag{9}$$

for sample 1, and

$$\Delta\rho^2 = \left[\rho_{\rm cc} - \frac{5.76w(w-0.01)}{(w-0.0038)}\right]^2 \tag{10}$$

for sample 2.

IANS experiments were performed at $0.125 < q < 0.205\,{\rm \AA^{-1}}$, where $I_{\rm inc}$ is dominant because the intensity profile is q-independent. Note that the recorded N is proportional to $I_{\rm inc}$, thus N is also proportional to the total volume fraction of hydrogen atoms, $\phi_{\rm H}$, in the sample irradiated by incident neutron, and not related to structures, *i.e.*, $N(t) \propto \phi_{\rm H}(t)$. It should be also noted that $\phi_{\rm H}$ is mainly affected by the amount of protonated water (H_2O) but not D_2O, hence it is variable due to the evaporation in the case of sample 1, but no change in the case of sample 2; $\phi_{\rm H}$ is also affected by the number of the hydrogen atoms covalently bonded to MC chains, which is variable as well due to the dimensional shrinkage in both cases of samples 1 and 2.

3 Results

3.1 Macroscopic shrinkage and time-resolved weighing measurement

A step-wise shrinking of the sample is clearly observable to eyes, which allows us to divide the drying process into three time regions: regions I, II and III. In region I, 3-dimensional shrinkage occurs: the height, width and thickness of the sample simultaneously decrease with time. At the end of region I, the cross area of the sample becomes $36 \times 27\,{\rm mm^2}$, and the sample thickness decreases down to $\sim$ 75% of x_0. In region II, 1-dimensional shrinkage is observed, where the height and width of the sample are retained, but the thickness of the sample further decreases. In region III, the appearance of the sample remains unchanged with time. Note that the boundary between regions I and II observed here will be confirmed by the quantitative analysis of N in conjunction with fig. 8b in sect. 3.4.

Accordingly, time-evolution of $W(t)$ for samples 1 and 2 as shown in figs. 2a and b, respectively, is divided into three time regions, as designated by broken lines. At the end of region I, $W(t)$ of both samples decreases to $\sim 60\%$. At the end of region II, $W(t)$ decreases further to $\sim 3.5\%$ for sample 1 and to $\sim 1.35\%$ for sample 2, respectively. In region III, $W(t)$ does not change with time any more, indicating that the drying is completed.

The end-up time ($t_{\rm end}$), which is defined as the time boundary between regions II and III, is different for the two samples, *i.e.*, $t_{\rm end,1} \sim 450\,{\rm min}$ for sample 1 and $t_{\rm end,2} \sim 550\,{\rm min}$ for sample 2. However, the residual weight fraction at the end of region I, $W_{\rm I}$ (= 60%), is found to be same for both samples. If we renormalize time t with $t_{\rm end}$ by introducing a shift factor β, which shifts an observation t relative to sample 1. For sample 2, $\beta = t_{\rm end,1}/t_{\rm end,2} = 0.818$. $W(t)$ for the two samples are plotted as a function of a reduced time, βt, in fig. 2c. The renormalized two curves superpose to each other, indicating that the mechanisms of drying for both samples are identical. Thus $W_{\rm I}$ is believed to be a characteristic value independent of the molecular weight of water (either H_2O or D_2O) rising from the different strength of H-bonding or D-bonding in the sample, and is determined solely by the nature of the sample itself.

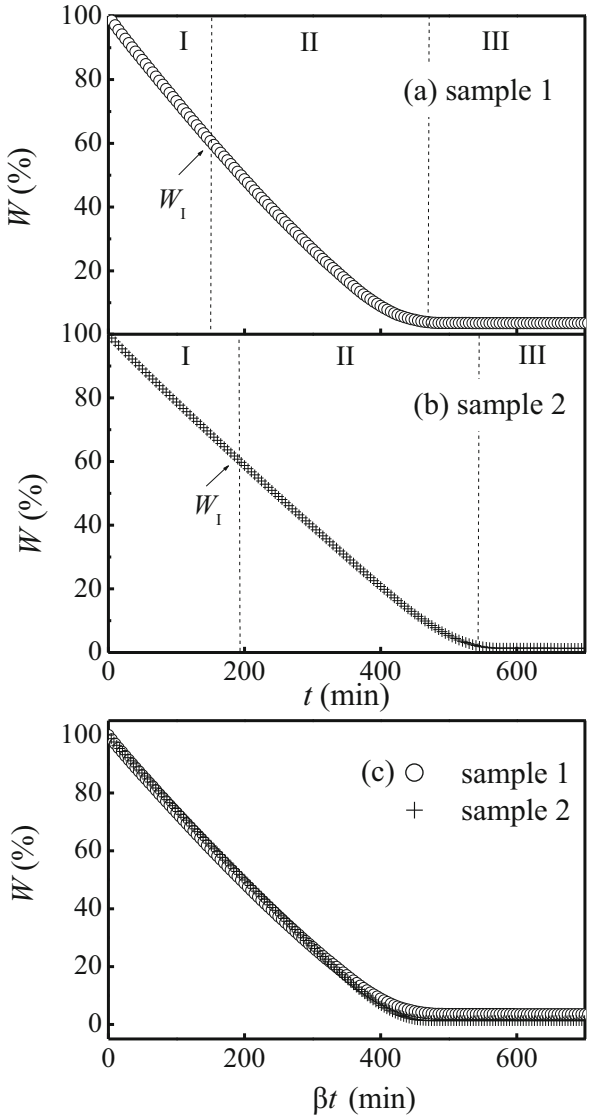

Fig. 2. Time dependence of W for (a) sample 1; (b) sample 2, during the natural drying process. The vertical broken lines indicate the time at the end of region I and II, respectively, as in later figures. (c) Reduced-time dependence of W for sample 1 and 2, respectively. β is the shift factor, defined by $\beta = t_{\mathrm{end},1}/t_{\mathrm{end},2} = 0.818$, as detailed in the text.

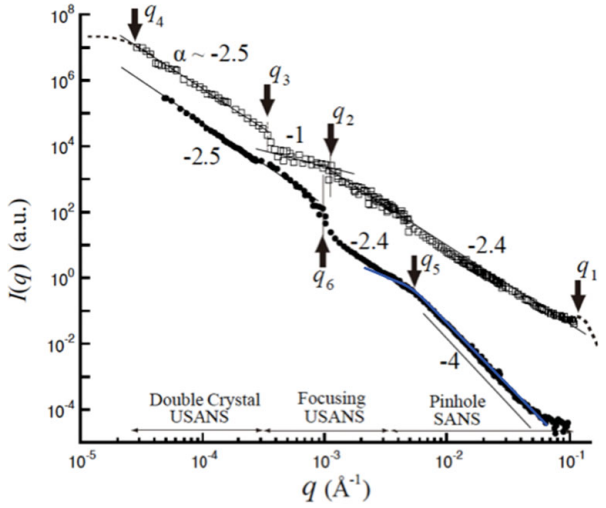

Fig. 3. Combined USANS and SANS profiles for sample 3 before (open squares) and after (solid circles) drying by vacuum.

3.2 Time-resolved neutron scattering

3.2.1 Hierarchical structure of MC at the length scales from 7 nm to 10 μm

Due to the limitations of the structure probes, the detailed supermolecular structure of cellulose is still open. The arrangement of the crystalline cellulose microfibrils in plants has been studied before. For instance, Jakob and co-workers reported that the wood cell wall of *Picea abies* is built with elementary cellulose filbrils with a uniform thickness, which was shown by compatible results investigated by three experimental techniques: transmission electron microscopy (TEM), wide-angle X-ray scattering (WAXS) and small-angle X-ray scattering (SAXS) [33]. Their SAXS data showed a clear minimum at $q \sim 0.3\,\text{Å}^{-1}$, which in turn gave the size of mean thickness of the fibrillar unit of 25 Å. Muller and co-workers reported a nearly perfect alignment of the microfibrils parallel to the fibril axis in native flax by means of position-resolved microbeam SAXS [34]. They pointed out that fibril is built up homogeneously in the sense that mean diameter and spacing as well as tilt angle of the microfibrils are uniform over the whole fibril cross section. Furthermore, they found a marked difference between SAXS patterns of dry and wet fibers. In both studies, SAXS intensity profiles were curved in the instrumentally reachable q range (0.02–$0.45\,\text{Å}^{-1}$) on the double logarithmic plot with q, and the shape of cellulose microfibrils was well approximated by a cylinder with a size distribution.

In the case of MC, we have reported the hierarchical arrangement of MC microfibrils in a very wide q range [4, 5]. Unlike the previous studies on the plant cellulose samples, the scattering profile of MC is found to always follow power law functions at different q-regions. In this section, we indicate the structural difference between the wet and dried MC samples according to these power law behaviors. The combined double-crystal USANS and focusing USANS intensity profiles for sample 3 before (hollow squares) and after complete drying by vacuum (solid circles) are shown in fig. 3. $I(q)$ *vs.* q is given by

$$I(q) \sim q^{-\alpha}, \tag{11}$$

where α is the q-dependent power law exponent, representing the fractal dimension at the representative length scale. The discussion of α at different q-regions has been detailed in ref. [4], and so here we would like to omit that part and simply mention the structures it relates to.

Before drying, the upper and lower cutoffs for the power laws are denoted as $q_1 \sim 0.1\,\text{Å}^{-1}$, $q_2 \sim 1 \times 10^{-3}\,\text{Å}^{-1}$, $q_3 \sim 3 \times 10^{-4}\,\text{Å}^{-1}$ and $q_4 \sim 3 \times 10^{-5}\,\text{Å}^{-1}$, respectively.

1) $\alpha \sim 2.4$ at $q_2 < q < q_1\,\text{Å}^{-1}$, is due to the concentration fluctuations of the cellulose crystallites in a bundle. The hump appearing at q_1 indicates the mean dimension of the cellulose crystallites is ~ 70 Å $(= 2\pi/q_1)$, in good agreement with the data in the previous work [35–38], especially corresponding to the diameter of fibril measured by WAXS and TEM techniques, such as 84 Å reported by Haase *et al.* [37], and 50–90 Å reported by Fink *et al.* [38]. All these data are found to be larger than the crystallite dimensions of 20–40 Å found in wood cells [39–41].
2) $\alpha \sim 1$ at $q_3 < q < q_2\,\text{Å}^{-1}$, is due to the rod-shaped cellulose bundle; q_2 is the upper q-limit for $\alpha = 1$, indicating that a cross section size of the bundle is ~ 600 nm $(= 2\pi/q_2)$.
3) $\alpha \sim 2.5$ at $q_4 < q < q_3\,\text{Å}^{-1}$, represents the cellulose network structure composed of bundles with lower and upper cutoff size of $\sim 2\,\mu$m $(= 2\pi/q_3)$ and $\sim 20\,\mu$m $(= 2\pi/q_4)$, respectively.

The α value and its applicable q range for the completely dried sample varied from the results of the wet sample mentioned above. The upper and lower q limits for power laws are denoted as $q_5 = 5 \times 10^{-3}\,\text{Å}^{-1}$ and $q_6 = 8 \times 10^{-4}\,\text{Å}^{-1}$.

4) $\alpha \sim 4.0$ at $q > q_5\,\text{Å}^{-1}$, is a typical Porod law exponent [42], arising from a sharp interface between cellulose crystallites and amorphous domains, which is very different from the q-behavior of the wet sample in the same q range as described in 1). The lower cutoff size is found to be ~ 125 nm $(= 2\pi/q_5)$, which is close to the width of the dried cellulose ribbon reported [27].
5) $\alpha \sim 2.4$ at $q_6 < q < q_5\,\text{Å}^{-1}$, is the same as that of the wet sample in the same q range mentioned in 1), implying that the concentration fluctuation of cellulose crystallites in the bundle, is similar to that of the wet sample.
6) $\alpha \sim 2.5$ at $q < q_6\,\text{Å}^{-1}$, is due to the same network structure as the structure mentioned in 3) of the wet sample. But the lower q limit shifted from q_3 to q_6 due to the shrinkage of the network upon drying. This shift superposes the q-range where we observed $\alpha = 1$ in the wet state, hence $\alpha = 1$ is no longer observed here. If we compare q_3 and q_6, we obtain a swelling ratio of sample 3, $\gamma = (q_6/q_3) \sim 2.7$.

3.2.2 Structural change induced by drying methods at $q > q_5\,\text{Å}^{-1}$

The results shown in sect. 3.2.1 reveal that the rapid drying process by vacuum dramatically changed the microscope structure at the length scale of 7 nm $\sim$ 125 nm $(q > q_5\,\text{Å}^{-1})$. In this section, we will focus on this length scale and elucidate the structural change induced by different drying methods.

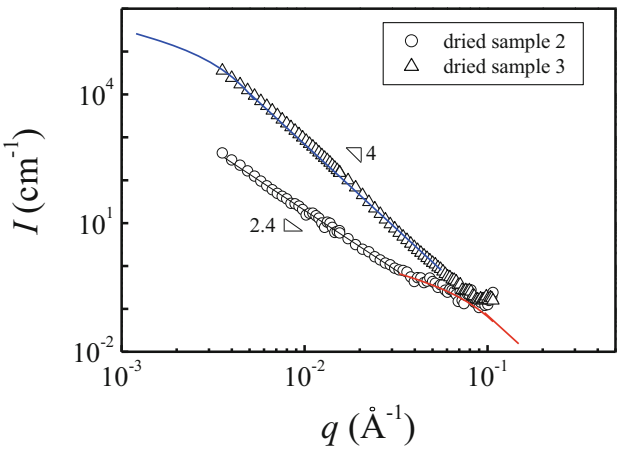

Fig. 4. Highlight of the SANS profiles at $q > q_5$ for naturally dried sample 2 (open circles) and rapidly dried sample 3 (open triangles). The red and blue solid lines show the best-fitted theoretical Guinier curves for these samples, respectively.

Figure 4 highlights the scattering profiles of naturally dried sample 2 (open circles) and rapidly dried sample 3 (open triangles) at $q > q_5\,\text{Å}^{-1}$. $I(q)$ *vs.* q obeys eq. (11) for both samples, except for the q-behavior of sample 2 at $q > q_g$, where $q_g \sim 0.03\,\text{Å}^{-1}$. α is 2.4 for sample 2, the same as the value in the wet state, whereas it is 4 for dried sample 3, which is the Porod law exponent and has been mentioned in 4) of sect. 3.2.1.

The scattering profile of sample 2 at $q > q_g$ reflects the structure of cellulose crystallite after natural drying. To estimate the effective size of the cellulose crystallites, a typical Guinier function [31,32] plot is used to fit the scattering profile at $q > q_g$, where

$$I(q) \sim \exp(-R_g^2 q^2/3), \tag{12}$$

with R_g being the radius of gyration of the crystallites. The best fitting result is shown by the solid red line in fig. 4, and the estimated R_g is ~ 25 Å.

The Guinier region for sample 3 after rapid drying is extended to $q < q_5$, which is beyond the SANS set-up in fig. 4. In order to know the effective size of the crystallites in the dried sample 3, we analyzed the scattering profile of the dried sample 3 in fig. 3, where the USANS and SANS data were combined together and Guinier region was easily found, and the estimated R_g is ~ 480 Å. The fitting curve is shown by solid blue line in fig. 3 and 4.

Note that for both dried samples, no matter by natural drying method or by rapid drying method, the observed size of the crystallites are larger than that in the wet sample, indicating that the drying induces the further crystallization and aggregation of the cellulose fibrils, hence bigger crystallites are formed. In contrast to the natural drying method, the rapid drying method results in even larger crystallites, possibly because cellulose fibrils stack

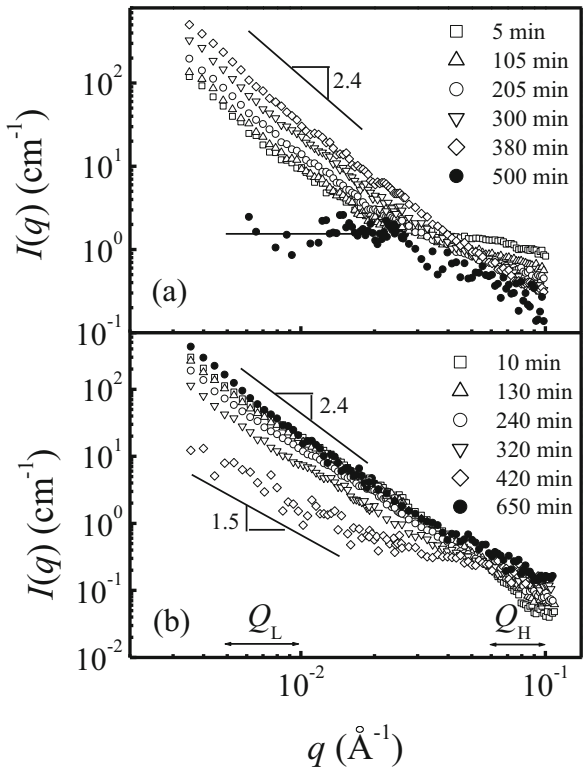

Fig. 5. Time evolution of SANS profiles at representative times for (a) sample 1; (b) sample 2 during the natural drying process.

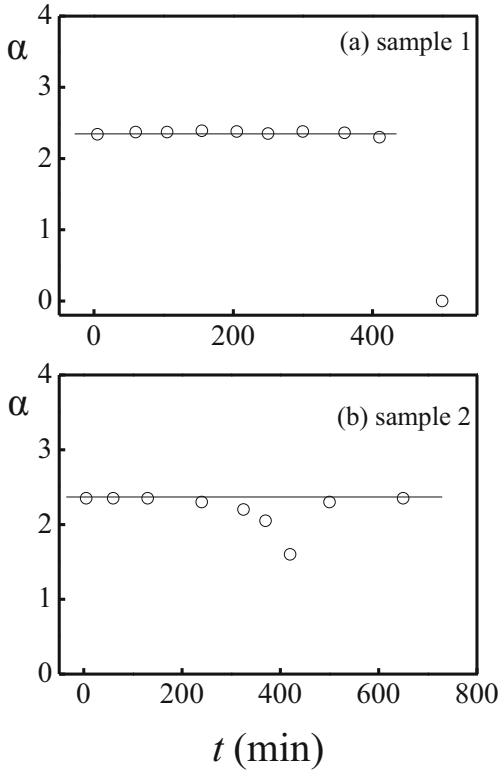

Fig. 6. Time dependence of α for (a) sample 1; (b) sample 2 during the natural drying process.

more quickly in the process due to less help from the presence of the solvent. The drying-induced crystallization and aggregation were also confirmed by our preliminary neutron diffraction experiment [30].

3.3 Time-resolved scattering measurement during the natural drying process

The microstructures of dried MC sample through different drying methods have been compared in sect. 3.2.2. In this section, we focus on the time-evolution of the structural change at $q > q_5\,\text{Å}^{-1}$ in the natural drying process. Two samples swollen in either protonated water(sample 1) or deuterated water (sample 2) are investigated.

Figure 5a shows the SANS profiles of sample 1 at representative time. At $0 < t < 380\,\text{min}$, $I(q)$ increases at $q < 0.04\,\text{Å}^{-1}$, while it decreases at $q > 0.04\,\text{Å}^{-1}$. After 380 min, $I(q)$ at all q suddenly decreases dramatically, and becomes very weak until the end.

The profiles obey eq. (11) well at $q < 0.04\,\text{Å}^{-1}$, corresponding to a length scale from 150 Å to 1500 Å. The α value obtained from each profile is plotted with time in fig. 6a. α equals 2.4 throughout the drying process, except for the final stage where it drops suddenly to ~ 0, which is due to the matching effect and will be discussed later in this section.

Figure 5b shows time-dependent scattering profiles of sample 2. Similar to sample 1, at $0 < t < 420\,\text{min}$, two opposite changes in $I(q)$ are observed at different q ranges: $I(q)$ decreases at $0.004 < q < 0.06\,\text{Å}^{-1}$, but increases at $q > 0.06\,\text{Å}^{-1}$. After 420 min, $I(q)$ suddenly increases dramatically, and is finally comparable to the initial state (*i.e.*, $t \sim 10\,\text{min}$) in the end. Profiles at $0.004 < q < 0.06\,\text{Å}^{-1}$ also obey eq. (11), thus α was calculated and plotted with t in fig. 6b. α is 2.4, except that it drops suddenly to ~ 1.6 at $t \sim 420$ min due to the matching effect.

The results in figs. 5a and b show that the SANS profiles of MC swollen by either H_2O or D_2O follow a common power law function with $\alpha = 2.4$, which indicates the microstructure of MC in the bundle is neither affected by the mass of water nor natural drying treatment.

Now let us consider the matching effect observed in both samples. Approaching the matching point, where $I(q)$ or $\Delta\rho^2$ is minimum, the averaged SLD of the amorphous regions matches the SLD of cellulose crystallites. If the match is perfect, $\alpha \sim 0$ is observed, this is the case for sample 1 shown in figs. 5a and 6a. If the match occurs quickly and $\Delta\rho^2$ immediately increases across the matching point, $\alpha < 2.4$ is observed, this is the case for sample 2 shown in figs. 5b and 6b.

In order to quantitatively investigate the time change in SANS profiles, it is useful to select a proper range at low q and high q regions, which are designated by the two arrows labeled Q_L and Q_H in fig. 5, to evaluate

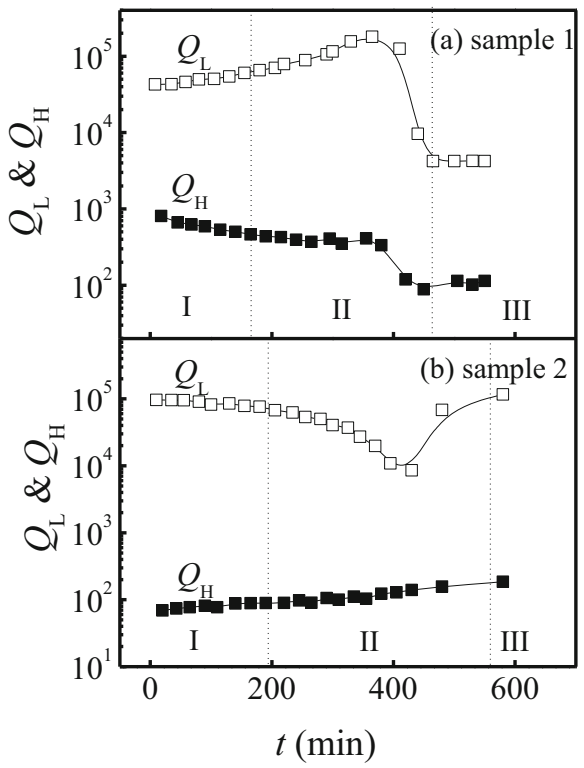

Fig. 7. Time dependence of Q_L and Q_H for (a) sample 1; (b) sample 2 during the natural drying process, where Q_L and Q_H are the respective characteristic scattering intensity in the low and high q regions designated by the two arrows in fig. 5, and defined in eqs. (13) and (14).

a characteristic scattering intensity, defined by

$$Q_L \equiv \int_{q_{L1}}^{q_{L2}} I(q)\mathrm{d}q / \int_{q_{L1}}^{q_{L2}} \mathrm{d}q, \quad (13)$$

$$Q_L \equiv \int_{q_{H1}}^{q_{H2}} I(q)\mathrm{d}q / \int_{q_{H1}}^{q_{H2}} \mathrm{d}q, \quad (14)$$

where $q_{L1} = q_5$, $q_{L2} = 0.01\,\text{Å}^{-1}$, $q_{H1} = 0.06\,\text{Å}^{-1}$, and $q_{H2} = 0.1\,\text{Å}^{-1}$.

The time dependence of Q_L and Q_H is presented in fig. 7a for sample 1 and fig. 7b for sample 2, respectively. In fig. 7a, at $0 < t < 380\,\text{min}$, Q_L increases but Q_H decreases continuously; at $t > 380\,\text{min}$, both of them suddenly decrease. In fig. 7b, Q_L decreases smoothly until 400 min, then increases rapidly. However, Q_H steadily increases throughout the whole process. We will quantitatively discuss Q_L and Q_H in conjunction with fig. 9 in sect. 4.3.

3.4 Time-resolved incoherent scattering measurement during the natural drying process

Figure 8a shows the time dependence of N for sample 1 measured by IANS. According to the 3-regions definition

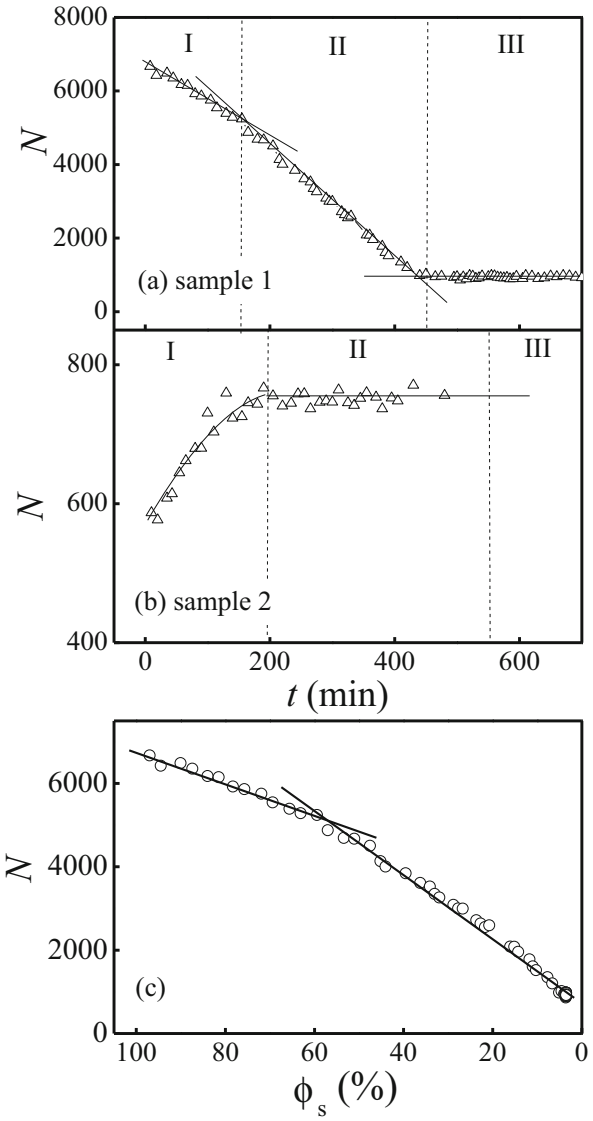

Fig. 8. Time dependence of N for (a) sample 1; (b) sample 2 during the natural drying process. (c) N *vs.* ϕ_s for sample 1. The solid lines drawn in panels (a) and (b) are only for visual guides, whereas the ones in panel (c) are the best-fitted lines given by eq. (15).

in the macroscopic observations mentioned in sect. 3.1, N is found to continuously decrease with time in both regions I and II, and becomes constant in region III. Note that although time dependence of N apparently shows continuous change in either region I or II, it does not mean that the macroscopic shrinkage of the MC membrane during the drying process is homogenous. The change of N with time is generally complicated and varies case by case. However, since N represents the relative incoherent intensity, it is always proportional to the volume fraction of hydrogen, ϕ_H, of the system [31,32]. Thus the plot between N and ϕ_H is believed to be linear and their slope enables us to estimate the rate of evaporation of water (or change of ϕ_H) at different time regions.

In the case of sample 1, the decrease in N should be attributed to two factors as we mentioned in sect. 2.3: i) the loss of H_2O upon drying; ii) the 3-dimensional shrinkage of the sample. Factor i) decreases N, due to the reduced number of hydrogen atoms when H_2O evaporates, whereas factor ii) increases N, due to the more hydrogen atoms covalently bonded on MC being brought up in the beam by shrinkage. Note that 1-dimensional shrinkage along the sample thickness has no contribution to N. Since factor i) is dominant and outweighs factor ii) because of the large weight fraction of H_2O in the sample, it is reasonable to assume that ϕ_H is the volume fraction of the solvent: H_2O, *i.e.*, $\phi_H \sim \phi_s$, where ϕ_s has been estimated by eq. (2). Thus N can be given by

$$N = A + B\phi_H \sim A + B\phi_s, \tag{15}$$

where A and B are fitting parameters, representing N of the residual MC sample at the end of each time region and the decrease rate of N with ϕ_s, respectively. In fig. 8c, we plot N as a function of ϕ_s. Equation (15) works well in both regions I and II. The best fitting results show $A = 2868$, $B = 39.5$ in region I, and $A = 695$, $B = 78.5$ in region II. The B value in region I is found to be about half of that in region II, because in region I, 3-dimensional shrinkage occurs and the effect of factor ii) increases the effective N and retards the effect of factor i), consequently decreases the rate of N; while in region II, 1-dimensional shrinkage occurs instead and only the factor i) itself determines N, hence B is larger. It should be noted that the linear relationship in eq. (15) is simply based on the scattering theory, but is not related to the heterogeneity in the macroscopic shrinkage of the MC membrane.

Figure 8b shows the time change in N for sample 2 by drying. Unlike that in fig. 8a, N increases continuously with time in region I, and then shows a constant value in both regions II and III, though the weight loss in sample 2 is continuous until the end of region II. Since D_2O makes no contribution to N, the change in N is practically caused by the effect of factor ii) only. The 3-dimensional shrinkage leads to the increase in N in region I, but in region II, 1-dimensional shrinkage does not affect N. Thus a clear cut between regions I and II defined by the macroscopic observation is evidenced by the quantitative change in N here. Note that sample 1 contains non-evaporated hydrogen-rich organic compounds, which gives a slightly larger N than that of sample 2 at the end of the drying process, though samples 1 and 2 are regarded to be biologically identical.

4 Discussion

In this section, we will first quantitatively calculate Q_L and Q_H based on the scattering theory, then will compare two cellulose samples 1 and 2 and summarize the similarities and difference between them, and finally will combine all quantities and analyze the changes according to the same time span from region I to III.

4.1 Quantitative calculations of Q_L and Q_H

In the q region at $q < 0.06\,\text{Å}^{-1}$ in fig. 5, the microstructure of MC does not change with time, therefore, $S(q)$ and $F(q)$ in eq. (4) are time-independent, the change in the scattering intensity is only attributed to the front factor given by

$$Q_L \propto \Delta\rho^2\phi_{cc}(t)[1 - \phi_{cc}(t)]. \tag{16}$$

Bringing eqs. (7), (9) and (10) back to (16), we have

$$Q_L \propto 0.0038 \times \left[\rho_{CC} + \frac{0.56w(w-0.01)}{(w-0.0038)}\right]^2 (W-0.0038)/W^2 \tag{17}$$

for sample 1, and

$$Q_L \propto 0.0038 \times \left[\rho_{CC} - \frac{5.76w(w-0.01)}{(w-0.0038)}\right]^2 (W-0.0038)/W^2 \tag{18}$$

for sample 2. We theoretically calculate Q_L as a function of time by using eqs. (17) and (18) with ρ_{cc} being the only unknown parameter, and compare the theoretical curve (shown in solid red lines) with the experimental Q_L data in figs. 9b and d. The best fit of the experimental data to the theoretical equations yields $\rho_{cc} \sim 0.9 \times 10^{10}\,\text{cm}^{-2}$. This will be discussed in detail in conjunction with other parameters together in sect. 4.3.

4.2 Similarities and difference between two cellulose samples

Since samples 1 and 2 were cut from the same pellicle, it is believed that the arrangement of cellulose microfibrils is biologically identical. This is evidenced by the universal curve shown in fig. 2c and the same q-behavior in figs. 5a and b, revealing the same nature of the cellulose fibrils in both samples. However, the different residual weight at the end of the drying process indicates the main difference between two samples: some organic molecules in the culture solution remained with sample 1, but were removed for sample 2. On the other hand, before drying, sample 1 contains lots of hydrogen atoms rising from H_2O solvent, but sample 2 contains deuterium atoms instead, since H_2O has been replaced to D_2O in the sample preparation step. The hydrogen-rich components such as organic compounds and H_2O molecules on one hand influence N in IANS measurements; on the other hand the non-evaporable organic compounds even affect the matching results, *i.e.*, α value when approaching the end of the drying process, because these components have the similar SLD as the cellulose and their existence makes the scattering contrast close to 0. Consequently, α has a discrete jump to 0 in sample 1 when drying is over as has been described in sect. 3.3 in conjunction with fig. 6a. Based on the discussion above, the similarity and difference between two samples are summarized in table 1.

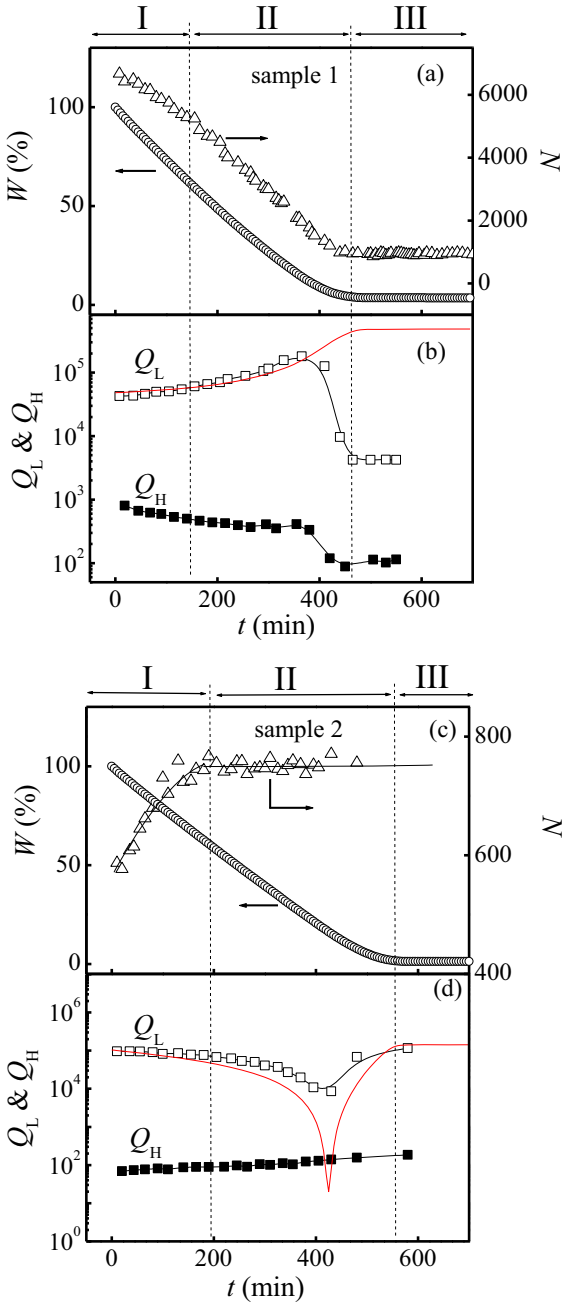

Fig. 9. Summary of time dependence of the characteristic parameters plotted on the common time scale. (a) W and N, (b) Q_{L} and Q_{H} for sample 1 and (c) W and N, (d) Q_{L} and Q_{H} for sample 2, respectively. The time dependence of theoretical Q_{L} (red solid lines) calculated by eqs. (17) and (18) is also shown in panel (b) and (d), respectively.

4.3 Various quantities displayed on a common time axis

In this section we discuss in detail how the drying process influences the structure of the MC samples in two length scales:

i) macroscopic structure of the MC sample in terms of W and N;
ii) microscopic structures of the MC sample in terms of Q_{L} and Q_{H}.

Comparisons of the time changes in all the parameters on the common time scale are indispensable to gain deeper understandings of the structures mentioned above, and thus they are shown together in fig. 9a-d without regard for redundancies.

Region I. Figures 9a and c show the time dependence of W and N for samples 1 and 2. W decreases with time for both samples. N decreases with time for sample 1 due to the loss of H_2O, but increases for sample 2 due to a 3-dimensional shrinkage of the sample.

The opposite changes in Q_{L} and Q_{H} are shown for the two samples in figs. 9b and d, respectively. On one hand, the best fit of the experimental data to the theoretical eqs. (17) and (18) yields $\rho_{\mathrm{cc}} \sim 0.9 \times 10^{10}\,\mathrm{cm}^{-2}$ as mentioned above in sect. 4.1; On the other hand, the calculated SLD of cellulose crystallites by eq. (8), $\rho_{\mathrm{cc,cal}}$, is estimated to be $\sim 1.87 \times 10^{10}\,\mathrm{cm}^{-2}$, about two times larger than the fitting value ρ_{cc}. Note that there exists the bound water layer surrounding the surfaces of cellulose fibrils, hence the best-fitted ρ_{cc} is the averaged SLD of the "bound water-cellulose crystallites complex", denoted by "complex" hereafter. Since H_2O was supplied in the original culture solution, the bound water would be H_2O, which is proved to be unreplaceable by the D_2O used for washing or removed by the drying treatment [30]. Thus ρ_{cc} is given by

$$\rho_{\mathrm{cc}} = f_{\mathrm{cc}}\rho_{\mathrm{cc,cat}} + f_{\mathrm{H_2O}}\rho_{\mathrm{H_2O}} \tag{19}$$

where $f_{\mathrm{cc}} + f_{\mathrm{H_2O}} = 1$, with f_{cc} and $f_{\mathrm{H_2O}}$ being the volume ratio of cellulose crystallites and water in the "complex", respectively. Hence, $f_{\mathrm{cc}} \sim 0.6$ and $f_{\mathrm{H_2O}} \sim 0.4$ are deduced from eq. (19). Taking the original volume fraction of cellulose crystallites in the wet sample $\phi_{\mathrm{cc}}(0) = 0.0038$ into account, the original volume fraction of bound water of the "complex" in the wet sample, $\phi_{\mathrm{BW\text{-}com}}(0)$ $[= \phi_{\mathrm{cc}}(0) \times f_{\mathrm{H_2O}}/f_{\mathrm{cc}}]$, is estimated to be ~ 0.0025. Since both non-crystalline cellulose and crystalline cellulose fibrils have "bound water", the total amount of "bound water" in the wet sample, $\phi_{\mathrm{BW}}(0)$, is estimated to be ~ 0.004, according to the assumption of the cellulose crystallinity of 60%. This value is consistent with the value ($\sim 0.35\,\mathrm{wt}\%$) obtained from the weight measurement to be discussed in *region III* later. The consistent results from two different experiments evidenced not only the existence of the bound water layer, but also the validity of eqs. (17) and (18).

A deviation between the fitting line and experimental data of Q_{L} is observed at the late stage of *region II* in fig. 9b because of the "matching effect" of the organic compounds to cellulose crystallites, and will be discussed in detail in *region II*.

Note that incoherent scattering intensity of sample 1 is very strong and dominantly responsible for the high Q_{H} in fig. 9b. The loss of H_2O with time leads to the decrease in Q_{H}. However, the incoherent contribution of D_2O in sample 2 is negligible [31,32], therefore, the increase in Q_{H} in fig. 9d reflects the possible structural change: more cellulose crystallites are formed during the drying process. This result is in good agreement with our preliminary WAXS

Table 1. Similarities and difference between two cellulose samples 1 and 2.

	Arrangement of cellulose microfibrils	Solvent	Solvent contribution to N	Organic compounds	Effect of organic compounds on α
Sample 1	same	H_2O	yes	yes	yes
Sample 2	same	D_2O	no	no	no

result that an increase of the crystallinity was founded [30] and also with the previous report by Zhang *et al.* [22].

Region II. W further decreases. N also decreases for sample 1 due to the continuous loss of H_2O, but has no change for sample 2. The constant N value for sample 2 means the total number of hydrogen atoms in the given scattering volume does not change any more. We therefore conclude that the shrinkage across the neutron beam stops, but that the shrinkage along the beam does proceed.

The same arguments of Q_L and Q_H in region I are positively applied here in region II as well, because of the continuous change across the boundary between regions I and II. However, in the late stage of region II, except Q_H for sample 2, a discrete decrease commonly appears in Q_L or Q_H in figs. 9b and d, indicating an approach to the matching point, where $\Delta\rho$ is near zero, therefore either Q_L or Q_H is very small. Basically, across the matching point, $\Delta\rho$ increases again, thereby raising the scattering intensity, as Q_L does in fig. 9d, however, Q_L or Q_H of sample 1 never increases beyond the matching point, and a big deviation between the theoretical curve and the experimental data is observed. This is possibly due to the fact that the organic compounds left in the solvent of sample 1, such as glucose, yeast and peptone, stick on the cellulose fibrils and become trapped in network meshes upon drying. $\Delta\rho$ between the cellulose crystallites and organic compounds is presumed to be very small because of the similar chemical structures, hence a match between them leads to a small Q_L or Q_H in sample 1. The organic compounds are non-evaporable, therefore, Q_L or Q_H never increases.

A continuous increase in Q_H is observed in fig. 9d, even across the matching point, because the intensity enhancement due to the growth of crystallites overweighs the intensity decrease due to the matching effect. As a consequence, matching effect was not observed in Q_H.

Region III. In this region, all the parameters are invariable, indicating the drying process is over. W ends up at $\sim 3.5\%$ for sample 1, but $\sim 1.35\%$ for sample 2. We assume the evaporation mechanisms for H_2O and D_2O are identical, thus the different residual weight fraction is due to the contribution of the residual organic compounds, which do not evaporate under the current experimental condition. The organic compounds weigh considerably in sample 1, while they are negligible in sample 2 because of the long time spent washing.

Considering the weight fraction of a completely dried sample of $\sim$ 1% wt [43,44], sample 2 still contains 0.35 wt% water after drying, which is believed to be "bound water". This result is consistent not only with the calculation of $\phi_{BW}(0)$ in region II but also the early reports [43,44].

5 Conclusion

The structure and structual change in the microbial cellulose sample during the drying process were investigated by a simultaneous measurement of time-resolved small-angle neutron scattering (SANS), intermediate-angle neutron scattering (IANS) and weighing techniques. Differing from the conventional studies, the scattering contrast between the cellulose crystallites and the amorphous regions automatically varied upon drying, allowing us to perform contrast variation without any extra procedures. The combined time-resolved studies enabled us to elucidate the structure and structural change of the MC sample in two different length scales on a rigorously common time scale: microscopic structure as shown by the parameters Q_L and Q_H obtained by SANS, and the macroscopic structure as shown by the parameters N and W obtained by IANS and weighing measurements.

Owing to this unique experimental methodology, all the experimental findings as described in the discussion section may be directly observed unequivocally. The results imply the following: the natural drying process involves three time regions: 3-dimensional shrinkage in region I, 1-dimensional shrinkage along the thickness of the sample in region II, and the completion in region III. The transition from 3-dimensional shrinkage to 1-dimensional shrinkage upon drying is evidenced by the change of N in IANS measurement for D_2O-swollen sample (sample 2), and attributed to the characteristic layer-by-layer structure of the cellulose network. In region III, "bound water" is found to be ~ 0.35 wt% in the weighing measurement, which has been also confirmed by the quantitative analysis on Q_L in SANS. In contrast to the natural drying process, the rapid drying by vacuum leads to crucial structural changes in a length scale of $7 \sim 125$ nm.

References

1. Y. Nishi, M. Uryu, S. Yamanaka, K. Watanabe, N. Kitamura, M. Iguchi, S. Mitsuhashi, J. Mater. Sci. **25**, 2997 (1990).
2. S.M. Keshk, Bioproces. Biotechniq. **4**, 1000150 (2014).
3. M. Shoda, Y. Sugano, Biotechnol. Bioprocess Eng. **10**, 1 (2005).

4. S. Koizumi, Y. Zhao, Y. Tomita, T. Kondo, H. Iwase, D. Yamaguchi, T. Hashimoto, Eur. Phys. J. E **26**, 137 (2008).
5. S. Koizumi, Y. Tomita, T. Kondo, T. Hashimoto, Macromol. Symp. **279**, 110 (2009).
6. R.L. Legge, Biotechnol. Adv. **8**, 303 (1990).
7. P. Ross, R. Mayer, M. Benziman, Microbial. Rev. **55**, 35 (1991).
8. K. Watanabe, M. Tabuchi, Y. Morinaga, F. Yashinaga, Cellulose **5**, 187 (1998).
9. J. Shah, R.M. Brown, Appl. Microbiol. Biotechnol. **66**, 352 (2005).
10. B.R. Evans, H.M. O'Neill, V.P. Malyvanh, I. Lee, J. Woodward, Biosens. Bioelectron. **18**, 917 (2003).
11. M. Iguchi, S. Yamanaka, A. Budhiono, J. Mater. Sci. **35**, 261 (2000).
12. D. Klemm, U. Udhardt, S. Marsch, D. Schumann, Polymer News **24**, 377 (1999).
13. D. Klemm, D. Schumann, U. Udhardt, S. Marsch, Prog. Polym. Sci. **26**, 1561 (2001).
14. O.M. Alvarez, M. Patel, J. Booker, L. Markowitz, WoundsCompend. Clin. Res. Pract. **16**, 224 (2004).
15. J.D. Fontana, A.M. Desouza, C.K. Fontana, I.L. Torriani, J.C. Moreschi, B.J. Gallotti, S.J. Desouza, G.P. Narcisco, J.A. Bichara, F.X. Farah, Appl. Biochem. Biotechnol. **24**, 253 (1990).
16. J.D. Fontana, C.G. Joerker, M. Baron, M. Maraschin, A.G. Ferreira, I. Torriani, A.M. Souza, M.B. Soares, M.A. Fontana, M.F. Guimaraes, Appl. Biochem. Biotechnol. **63**, 327 (1997).
17. R. Jonas, L.F. Farah, Polym. Degrad. Stabil. **59**, 101 (1998).
18. P.L. Park, J.Y. Je, H.G. Byun, S.H. Moon, S.K. Kim, J. Microbiol. Biotechnol. **14**, 317 (2004).
19. A.M. Sokolnicki, R.J. Fisher, T.P. Harrah, D.L. Kaplan, J. Membr. Sci. **272**, 15 (2006).
20. US 4655758, Microbiol Polysaccharide articles and methods of production (1987).
21. C. Clasen, B. Sultanova, T. Wilhelms, P. Heisig, W.M. Kulicke, Macromol. Symp. **244**, 48 (2006).
22. C. Zhang, L. Wang, J. Zhao, P. Zhu, Adv. Mater. Res. **239-242**, 2667 (2011).
23. P. Ramanen, P.A. Penttila, K. Svedstrom, S.L. Maumu, R. Serimaa, Cellulose **19**, 901 (2012).
24. M. Schramm, S. Hestrin, Biochem. J. **56**, 163 (1954).
25. M. Schramm, S. Hestrin, J. Gen. Microbiol. **11**, 123 (1954).
26. S. Bielecki, A. Krystynowicz, M. Turkiewicz, A. Kalinowska, *Bacterial Cellulose*, Biopolymers Online (2005), DOI: 10.1002/3527600035.bpol5003.
27. C.Q. Sun, J. Pharm. Sci. **94**, 2132 (2005).
28. S. Koizumi, H. Iwase, J. Suzuki, T. Oku, R. Motokawa, H. Sasao, H. Tanaka, D. Yamaguchi, H. Shimizu, T. Hashimoto, J. Appl. Crystallogr. **40**, s474 (2007).
29. D. Yamaguchi, S. Koizumi, R. Morokawa, T. Kumada, K. Aizawa, T. Hashimoto, Physica B. **385-386**, 1190 (2006).
30. S. Koizumi, Y. Zhao, Y. Tomita, D. Yamaguchi, H. Iwase, R. Motokawa, T. Hashimoto, T. Kondo, Soft Matter, submitted.
31. R.J. Roe, *Methods of X-ray and Neutron Scattering in Polymer Science* (Oxford University Press, New York, 2000).
32. J.S. Higgins, H.C. Benoit, *Polymers and Neutron Scattering* (Clarendon Press, Oxford, 1994).
33. H.F. Jakob, D. Fengel, S.E. Tschegg, P. Fratzl, Macromolecules **28**, 8782 (1995).
34. M. Muller, C. Czihak, G. Vogl, P. Fratzl, H. Schober, C. Riekel, Macromolecules **31**, 3953 (1998).
35. C.H. Haigler, P.J. Weimer (Editors), *Biosynthesis and Biodegradation of Cellulose* (Marcel Dekker, New York, 1991).
36. N. Lavoine, I. Desloges, A. Dufresne, J. Bras, Carbohydr. Polym. **90**, 735 (2012).
37. J. Haase, R. Hosemann, B. Renwanz, Colloid Polym. Sci. **252**, 712 (1974).
38. H.P. Fink, D. Hofmann, H. Purz, J. Acta Polym. **41**, 131 (1990).
39. H.F. Jakob, P. Fratzl, S.E. Tschegg, J. Struct. Biol. **113**, 13 (1994).
40. T. Nomura, T. Yamada, Wood Res. **52**, 1 (1972).
41. S. Andersson, R. Serimaa, T. Paakkari, P. Saranpää, E. Pesonen, J. Wood Sci. **49**, 531 (2003).
42. G. Porod, Kolloid Z. **124**, 83 (1951).
43. A. Okiyama, H. Shirae, H. Kano, S. Yamanka, Food Hydrocolloids **6**, 471 (1992).
44. A. Okiyama, M. Motoki, S. Yamanaka, Food Hydrocolloids **6**, 503 (1993).